Steering of an Underactuated Legged Robot through Terrain Contact with an Active Tail

Carlos S. Casarez[1] and Ronald S. Fearing[2]

***Abstract*— This paper analyzes and implements two novel turning strategies for underactuated legged robots that leverage contact of an active tail against terrain. The first strategy produces a sustained turn with a tail dragging against the ground during forward locomotion. The second strategy produces a rapid point turn by impacting the tail against the ground. LoadRoACH, a 55 g palm-sized legged robot, is developed to carry the active tail payload used in turning experiments. A steady-state turning model predicts the achievable turn speed of the robot on carpet, and open-loop turning experiments characterize the performance of the two tail contact turning strategies. Tail drag turning provides comparable turning maneuverability to differential drive turning gaits on carpet and gravel surfaces. Tail impact turning can produce rapid point turns on carpet, tarp, and gravel, but has a large variability in turn angle and time to recover from the turn. Finally, tail drag and tail impact turning control methods are implemented in an aggressive closed-loop corner steering maneuver.**

I. Introduction

Small, rapidly-manufactured legged robots have the potential to bring mobile sensing to various real-world environments. The diverse surfaces and granular media encountered in indoor and outdoor environments can be overcome with legged mobility, as demonstrated extensively by robots such as RHex [1], BigDog [2], and the MIT Cheetah 2 [3]. However, it is costly to deploy complex individual robots with many actuators to gather information for search and rescue tasks in disaster sites such as collapsed buildings.

The primary contribution of this paper is the analysis and experimental characterization of two novel turning strategies for tailed legged robots: dragging a tail against the ground to generate sustained turning forces while running, and impacting a tail against the ground to rapidly change heading.

The secondary contribution of this paper is the development of LoadRoACH (high payload Robotic Autonomous Crawling Hexapod), which is pictured in Fig. 1. LoadRoACH is a 55 g, palm-sized robot that is able to dynamically run while carrying payload equal to 50% of its body weight. In previous work, a precursor to this robot demonstrated improved mobility over terrain with steep drops [4]. The shell protects from impacts against the ground as the robot tumbles, and the tail enables rapid self-righting on various terrain types if the robot becomes inverted. With the same tail actuator that it uses for self-righting, LoadRoACH can turn by leveraging tail contact with the ground.

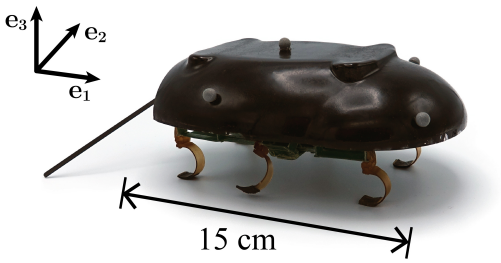

Fig. 1. LoadRoACH with two motors driving six legs and a single degree of freedom tail for tail-assisted dynamic turning.

The paper is organized as follows: Section II gives an overview of turning strategies and tail functionality of previous robots. Section III develops a model of sustained turning with a dragging tail and describes transient tail impact turning using experiment data. Section IV details the LoadRoACH with tail robot platform used in turning experiments. Section V presents open-loop experiments characterizing the turning performance of the tail contact turning strategies compared to a baseline of differential drive. Closed-loop steering results are also presented for an aggressive corner turn maneuver. Section VI discusses the achieved turning performance of the robot and lays out future work.

II. Background

Previous legged robots have employed a wide variety of turning strategies. Many robots implement kinematic turning strategies that adjust the position or velocity parameters of individual leg motions. Kinematic turning includes the online modification of Buehler clock parameters by RHex [1], phase adjustment of leg cycles by the HAMR microrobot [5], adjusting foot placement by iSprawl [6], and differential drive of motors driving multiple legs on each robot side by OctoRoACH [7]. Kinematic turning strategies may fail for robots running at faster speeds because they do not consider the dynamics of legged locomotion. Effective dynamic strategies for turning include active leg stiffness adjustment by RoACH [8], phase-locked roll turn gaits on VelociRoACH [9], and leveraging differential leg compliance while controlling the acceleration profile of legs connected to a single motor by 1STAR [10].

In addition to kinematic or dynamic modulation of legged gaits for turning, there are some methods that dedicate actuation to turning that is decoupled from leg actuation.

*This material is based upon work supported by an NSF Graduate Research Fellowship for Casarez, NSF CMMI Grant No. 1427096, and the United States Army Research Laboratory under the Micro Autonomous Science and Technology Collaborative Technology Alliance.

[1]Carlos S. Casarez is with the Department of Mechanical Engineering, University of California, Berkeley, CA 94720 USA. casarezc@berkeley.edu

[2] Ronald S. Fearing is with the Department of Electrical Engineering and Computer Sciences, University of California, Berkeley, CA 94720 USA. ronf@eecs.berkeley.edu

This can be especially useful for underactuated robots such as LoadRoACH that cannot directly control lateral leg forces. Turning strategies with dedicated actuators include TAYL-RoACH swinging an inertial tail in the yaw plane [11], the Dima wheeled robot balancing centripetal turning moments with an inertial roll tail to turn more rapidly [12], and SailRoACH turning with aerodynamic forces acting on a yaw tail [13].

Previous research on robots using tails for dynamic maneuvers focuses on inertial tail swings for rapid reorientation. Libby et al. developed a dynamic template for inertial reorientation with rotating limbs or tails [14] and the Salto jumping robot uses a balanced inertial tail to correct its attitude in the pitch direction [15]. Ground contact of tail-like or wing-like appendages for self-righting has been analyzed in depth by Kessens et al. [16] and Li et al. [17], but tail contact during legged locomotion has been relatively unexplored. Brill et al. analyzed and implemented dynamic legged leaps assisted by a tail on the Penn Jerboa [18]. In contrast, the robot platform in this work is used to explore how tail contact coupled with periodic dynamic running can enhance turning mobility.

III. Tail contact turning analysis

Two approaches are applied to the newly-developed tail contact turning strategies. First, an equilibrium analysis is performed on a simplified model of a legged robot turning in the yaw plane to determine the forward speed and angular velocity of steady-state tail drag turns. Next, experimental time trajectories of motion resulting from LoadRoACH impacting its tail against the ground are presented to qualitatively explain this turn method. In the following analysis, measured parameter values for the LoadRoACH robot are used.

A. Sustained tail drag turns

1) Formulation of steady-state turning equilibria: Free body diagrams of a legged robot performing a steady-state tail drag turn are shown in Fig. 2. The legs of the robot are assumed to drive the robot directly forward in the $\mathbf{e_1}$ direction at a speed of v_{Gx}, while it turns about its local vertical axis $\mathbf{e_3}$ at an angular rate of $\dot{\psi}$. In this steady-state analysis, the forces that act on the robot are assumed to cancel out so that the robot undergoes zero acceleration in translation and rotation about its body axes $(\mathbf{e_1}, \mathbf{e_2}, \mathbf{e_3})$ fixed to its center of mass (C.o.M.), except for the centripetal turning acceleration $\dot{\psi}^2 r\mathbf{e_2}$, where $r = v_{Gx}/\dot{\psi}$ is the turning radius. Gravitational force $m\mathbf{g}$ acts vertically downward (with total robot mass $m = 82$ g and $||\mathbf{g}|| = 9.81$ m/s^2), the compliant tail drags against the ground with force $\mathbf{F_t}$ satisfying Coulomb friction, and the legs produce a net force $\mathbf{F_b}$ within the robot's base of leg support. The body and tail forces act at contact locations of $\mathbf{r_{P,b}}$ and $\mathbf{r_{P,t}}$ respectively. The legs must produce enough force along the forward direction of travel to counteract the tail dragging force, and the legs and tail must produce a net cornering force towards the center of the turn $(\mathbf{e_2})$ to counteract the centripetal inertial force $m\dot{\psi}^2 r$ acting in the $-\mathbf{e_2}$ direction.

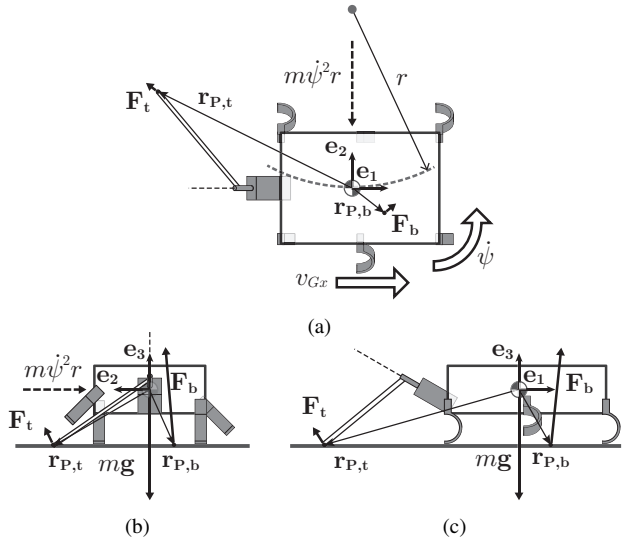

Fig. 2. Free body diagrams of (a) overhead, (b) back, and (c) side views of a legged robot performing a sustained turn while dragging a tail.

The force balance equations of the system are given below for the $\mathbf{e_1}$ (1), $\mathbf{e_2}$ (2), and $\mathbf{e_3}$ (3) directions:

$$m\dot{v}_{Gx} = 0 = F_{bx} + F_{tx} \quad (1)$$

$$m\dot{\psi}^2 r = F_{by} + F_{ty} \quad (2)$$

$$mg = F_{bz} + F_{tz}, \quad (3)$$

where the subscripts (x, y, z) denote $(\mathbf{e_1}, \mathbf{e_2}, \mathbf{e_3})$ components of $\mathbf{F_b}$ and $\mathbf{F_t}$. The moment balance equations are given below for the $\mathbf{e_1}$ (4), $\mathbf{e_2}$ (5), and $\mathbf{e_3}$ (6) directions:

$$m\dot{\psi}^2 r z_{P,t} = F_{bz} y_{P,b} + F_{tz} y_{P,t} \quad (4)$$

$$0 = F_{bz} x_{P,b} + F_{tz} x_{P,t} \quad (5)$$

$$0 = F_{by} x_{P,b} - F_{bx} y_{P,b} + F_{ty} x_{P,t} - F_{tx} y_{P,t}, \quad (6)$$

where $(x_{P,b}, y_{P,b}, z_{P,b})$ and $(x_{P,t}, y_{P,t}, z_{P,t})$ denote $(\mathbf{e_1}, \mathbf{e_2}, \mathbf{e_3})$ components of $\mathbf{r_{P,b}}$ and $\mathbf{r_{P,t}}$. Note that in these equations, (1) and (2) were applied. Also note that $z_{P,t} = z_{P,b}$ because the tail and legs both contact the horizontal ground plane.

In order to determine the possible velocities $(v_{Gx}, \dot{\psi})$ of steady-state turns depending on robot system parameters, the 6 force/moment balance equations of the system must be solved by reducing the system unknowns to 6. First, the tail contact location can be determined from the geometric parameters shown in Fig. 3. The C.o.M. position parameters are $(x_G, z_G) = (4.5, 3.5)$ cm and the tail base position parameters are $(x_m, z_m) = (-6.8, 4.2)$ cm. The tail motor is mounted at an angle $\alpha_m = 20^\circ$ about $\mathbf{e_2}$. The tail has length $l_t = 9$ cm, and is mounted so that it sweeps out a cone with angle $\beta_t = 20^\circ$ directed along the $-\mathbf{e_1^m}$ axis in the motor frame $(\mathbf{e_1^m}, \mathbf{e_2^m}, \mathbf{e_3^m})$. The tail motor rotates the tail with counterclockwise rotation angle θ_t. To determine the tail contact location, the tail angle to contact the ground θ_{t0} is computed from the tail geometry. Below, (7), (8), and (9) are the components of the tail contact location relative to the tail base in the motor frame. Because the tail base height

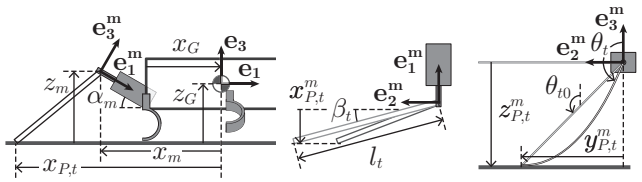

Fig. 3. Geometric parameters for tail drag turning with (a) side, (b) overhead motor frame, and (c) back motor frame views.

z_m is known from the robot geometry, (10) can be solved to determine $\theta_{t0} = 131°$ according to (11).

$$x^m_{P,t} = -l_t \sin\beta_t \tag{7}$$
$$y^m_{P,t} = l_t \cos\beta_t \sin\theta_{t0} \tag{8}$$
$$z^m_{P,t} = l_t \cos\beta_t \cos\theta_{t0} \tag{9}$$
$$z_m = x^m_{P,t} \sin\alpha_m - z^m_{P,t} \cos\alpha_m \tag{10}$$
$$\sin\left(\theta_{t0} - \frac{\pi}{2}\right) = \frac{z_m \sec\alpha_m + l_t \sin\beta_t \tan\alpha_m}{l_t \cos\beta_t} \tag{11}$$

From these tail geometry calculations, the contact locations have been determined and can be transformed to the body frame, with the exception of the $\mathbf{e_1}$ and $\mathbf{e_2}$ components of $\mathbf{r_{P,b}}$, which depend on moment balances. The tail force can be determined from the assumed relations below:

$$\mathbf{F_t} = -\frac{\mu_t F_{tz}}{||\mathbf{v_{P,t}}||}\mathbf{v_{P,t}} + F_{tz}\mathbf{e_3} \tag{12}$$
$$\mathbf{v_{P,t}} = (v_{Gx} - y_{P,t}\dot{\psi})\mathbf{e_1} + x_{P,t}\dot{\psi}\mathbf{e_2} \tag{13}$$
$$F_{tz} = k_t l_t \sin\Delta\theta_t, \Delta\theta_t = \theta_t - \theta_{t0}. \tag{14}$$

The components of $\mathbf{F_t}$ in the ground plane satisfy the Coulomb friction relation (12), which states that the magnitude of this planar force is the tail sliding coefficient of friction μ_t (0.7 on carpet) multiplied by the vertical tail force F_{tz} and its direction opposes $\mathbf{v_{P,t}}$ (13). The tail is compliant in bending about the motor rotation axis, which results in an applied spring force against the ground as θ_t increases past θ_{t0}. The magnitude of the vertical tail force follows the force-deflection relation in (14), with linear tail stiffness $k_t = 6.6$ N/m multiplying the vertical tail deflection $l_t \sin\Delta\theta_t$, where $\Delta\theta_t$ is positive as the tail deflects against the ground as shown in Fig. 3c.

Finally, an assumption is made on the robot's leg drive capabilities under loading. For a given gait and surface, the robot is assumed to run at a forward speed of v_{nl} under zero tail drag loading, which then linearly decreases to zero as the backward tail drag load decreases to $F_{tx} = -F_s$. For LoadRoACH running on carpet at a 10 Hz stride frequency, $v_{nl} = 70$ cm/s and $F_s = 0.3mg$. Because $F_{bx} = -F_{tx}$ from (1), this results in the force-speed relation below:

$$F_{bx} = F_s\left(1 - \frac{v_{Gx}}{v_{nl}}\right) \tag{15}$$

Applying the above constraints on forces and displacements, the force and moment balances (1)–(6) can be solved for the 6 unknowns $(x_{P,b}, y_{P,b}, F_{by}, F_{bz}, v_{Gx}, \dot{\psi})$.

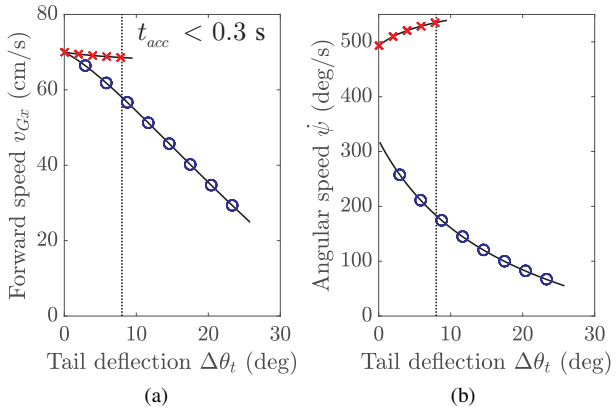

Fig. 4. Steady-state turning equilibria from the dynamic analysis of dragging a tail with frictional contact. For each tail angle deflection $\Delta\theta_t$, there exists either a stable steady-state turn (blue circles), an unstable steady-state turn (red X's), or no steady-state turn. (a) Forward velocity and (b) angular velocity for each turn.

2) Steady-state turning performance: The forward speed v_{Gx} and yaw angular velocity $\dot{\psi}$ of steady-state tail drag turns were determined as a function of tail deflection against the ground $\Delta\theta_t$. The results are shown in Fig. 4a and Fig. 4b. Stability analysis of the two determined solution branches revealed that the branch with higher turn velocities (marked by red X's) represents unstable equilibria, and the lower branch (marked by blue circles) represents stable equilbria. The stable branch represents physically achievable steady-state turns, in which the tail dragging force rejects perturbations from the turning equilibrium. As $\Delta\theta_t$ increases, the forward velocity of the steady-state turn decreases from the unloaded value of $v_{nl} = 70$ cm/s as the tail drag force increases according to the force-deflection relation of the tail and the tail-ground coefficient of friction $\mu_t = 0.7$. If $\Delta\theta_t$ exceeds 25°, the curves terminate. Past $\Delta\theta_t = 25°$, the applied vertical tail force would cause the body to tip (with $|y_{P,b}| > 3.5$ cm), which violates an assumption of the steady-state turning model. The minimum required leg-ground coefficient of friction to prevent slipping during the turn was determined to be 0.4, which is exceeded by the measured value of $\mu_b = 1.25$ for movement on carpet.

In order to apply the results of this steady-state tail drag turn analysis to an actual robot, dynamic conditions have to be applied to select a turn that is fast enough for rapid steering. To initiate turning, the robot runs straight forward and then touches its tail to the ground with a set tail deflection. Using an angular impulse-momentum calculation about the $\mathbf{e_3}$ axis, the time to accelerate into the turn is:

$$J_z\dot{\psi} = \int_0^{t_{acc}} M_z dt \tag{16}$$

Assuming the yaw moment M_z linearly decays from a maximum value of $M_{z,max} = \mu_t F_{tz} y_{P,t}$ to zero as the robot enters the turn, the time to accelerate can be approximated as $t_{acc} = \frac{2J_z\dot{\psi}}{M_{z,max}}$. If the robot is required to turn quickly, then there is a lower threshold on $\Delta\theta_t$ for tail drag turning that meets this acceleration constraint. In Fig. 4, the vertical dotted line at $\Delta\theta_t = 8°$ marks the threshold past which the

robot can initiate a tail drag turn faster than $t_{acc} = 0.3$ s. With a measured maximum tail motor rotation rate of 10 Hz during free run, the robot requires $t_{switch} = 0.073$ s to swing its tail through an angle $2\theta_{t0} = 262°$ to switch tail drag turn direction. These physical limitations of the robot system impose a time delay of $t_{acc} + t_{switch} = 0.373$ s before tail drag turning at the maximum projected speed can be achieved in the desired direction.

With a reasonable constraint on turning acceleration time, Fig. 4 predicts that the maximum tail drag turning performance of the robot system is bounded by an upper threshold of $v_{Gx} = 58$ cm/s and $\dot{\psi} = 180$ deg/s. However, this steady-state model does not consider that leg-ground interaction forces can impede yaw rotation of the robot. Therefore, a better prediction of the achievable $\dot{\psi}$ for tail drag turning is the value in Fig. 4 multiplied by an aerial duty factor $D_{aerial} \in [0, 1]$. As a baseline comparison, DASH runs with an aerial phase $D_{aerial} = 0.3$ [19], which results in a predicted tail drag turn rate of 54 deg/s.

B. Transient tail impact turns

1) Impulse-momentum applied to maneuver: A free body diagram of a legged robot performing a transient tail impact turn is shown in Fig. 5. As is qualitatively represented in the diagram, controlling to a commanded tail velocity $\dot{\theta}_{t,des}$ swings the tail into the ground, which generates large tail contact forces that act to rotate the robot with an angular velocity profile $\boldsymbol{\omega}(t) = \omega_x(t)\mathbf{e_1} + \omega_y(t)\mathbf{e_2} + \omega_z(t)\mathbf{e_3}$.

To analyze the net impulse applied by the combination of the tail and leg contact forces from collected experimental data, impulse-momentum theory is applied to the 3D rotational dynamics of the system:

$$\Delta L_x(t) = \int_0^t \left(J_x\dot{\omega}_x(\tau) + (J_z - J_y)\omega_y(\tau)\omega_z(\tau)\right) d\tau \quad (17)$$

$$\Delta L_y(t) = \int_0^t \left(J_y\dot{\omega}_y(\tau) + (J_x - J_z)\omega_x(\tau)\omega_z(\tau)\right) d\tau \quad (18)$$

$$\Delta L_z(t) = \int_0^t \left(J_z\dot{\omega}_z(\tau) + (J_y - J_x)\omega_x(\tau)\omega_y(\tau)\right) d\tau \quad (19)$$

where $(J_x, J_y, J_z) = (398, 1424, 1739)$ g-cm^2 are the mass moments of inertia of the robot about its body-fixed axes and the integrand expressions on the right hand sides of (17), (18), and (19) are the net moments acting on the robot in the $\mathbf{e_1}$, $\mathbf{e_2}$, and $\mathbf{e_3}$ directions. The result is the cumulative angular impulse during the maneuver $(\Delta L_x(t), \Delta L_y(t), \Delta L_z(t))$, which helps to visualize the effect of the impulsive moment that the tail applies to rotate the robot.

2) Experimental analysis: Robot telemetry from an experiment in which the robot impacted its tail against the ground while running forward on carpet is shown in Fig. 6. In this maneuver, the robot swung its tail counterclockwise to impact the ground at a commanded rotation rate of 8 Hz. For high-speed video of a similar experiment, refer to the video attachment. The telemetry data show that a 0.1 s duration negative step in the yaw impulse (ΔL_z) begins at a time of 0.55 s within the tail impact window (between the dotted

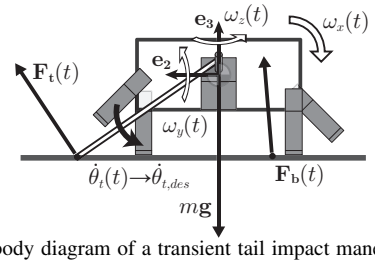

Fig. 5. Free body diagram of a transient tail impact maneuver causing 3D rigid body rotation of a legged robot.

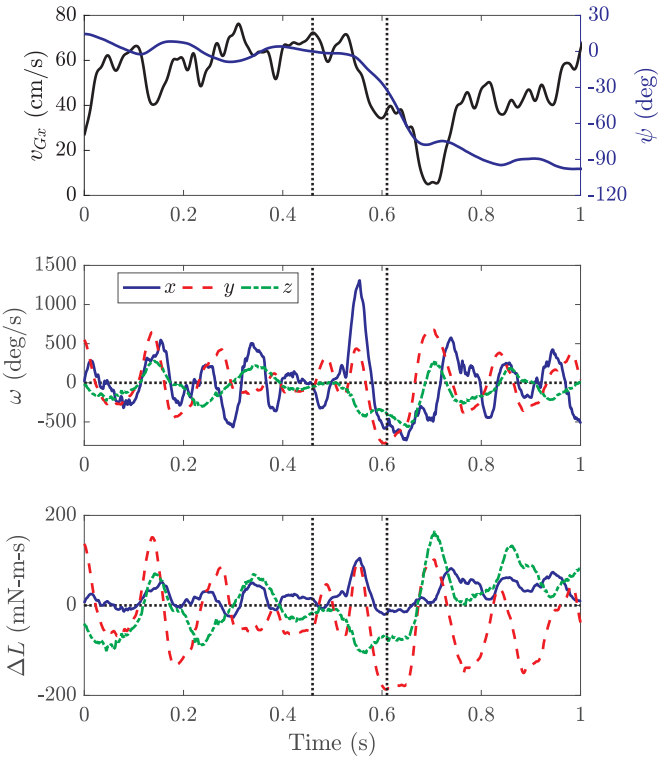

Fig. 6. Motion tracking and robot telemetry data during a transient tail impact turn on carpet. In this maneuver, the robot swung its tail counterclockwise at a commanded rotation rate of 8 Hz. Top: Forward velocity v_{Gx} measured from the motion tracking system (left axis, black line) and yaw angle ψ from Euler angle updates using the robot's gyroscope measurements (right axis, blue line). Middle: body-fixed angular velocity $(\omega_x, \omega_y, \omega_z)$ measured by the robot's gyroscope. Bottom: Cumulative body-fixed angular impulse $(\Delta L_x, \Delta L_y, \Delta L_z)$ calculated from the gyroscope time series data. The dotted vertical lines mark the start of the tail swing in the air and the moment when the tail completes a full rotation.

vertical lines), which acts to rotate the robot about $-\mathbf{e_3}$ with decreasing yaw angle ψ. Because the tail impacts the ground at a contact point that is offset from the robot C.o.M. in the $-\mathbf{e_1}$ and $\mathbf{e_2}$ directions, it produces pitch (ΔL_y) and roll (ΔL_x) impulses that aggressively pitch the robot forward and roll the robot to the right. After the tail impact, gravity restores the robot back to a level posture and it resumes a periodic running gait. The collected motion tracking data of the robot's forward velocity shows that the robot almost slows to a stop after the tail impact, and returns to its nominal running speed 0.55 s after the tail impact maneuver started. The net effect of the tail impact is a $\Delta\psi = -90°$ turn clockwise after $\Delta t = 0.55$ s. The experimentally determined value of Δt gives the delay before the tail impact fully

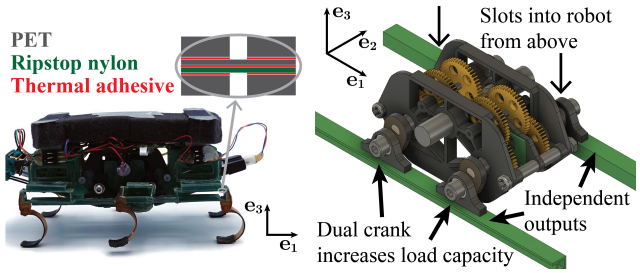

Fig. 7. Annotated images of LoadRoACH with improved flexure technology and transmission. (a) Side view image of the robot without shell, with detail showing structure and flexure material. (b) Isometric solid model view of the leg transmission module.

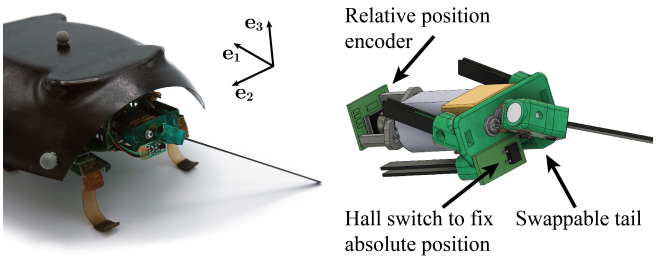

Fig. 8. Tail module for LoadRoACH. (a) Image of the tail module attached to the robot. (b) Solid model diagram of the isolated tail module.

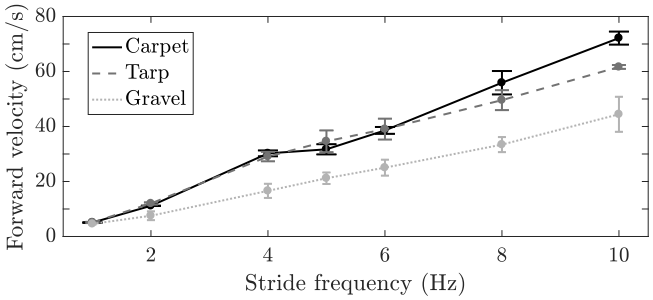

Fig. 9. Average forward velocity for alternating tripod gaits with varying stride frequency on different surfaces. The data points are experimental averages over 5 trials and the error bars show one standard deviation.

turns the robot and provides a reasonable constraint on the minimum feasible time interval between tail impact events. The effect of tail rotation rate on $\Delta\psi$ and Δt while running on different surfaces is characterized in Section V.

IV. Robot System

A. LoadRoACH

LoadRoACH maintains the SCM construction, dynamic gait, and differential leg drive of VelociRoACH [20] while improving its load capacity. Fig. 7 highlights the design changes to LoadRoACH compared to previous RoACH robots that enable it to carry a payload equal to 50% of its body weight. Previous folded millirobot designs used cardboard structural material and thin polyester (PET) or ripstop nylon flexures. LoadRoACH uses the composite structure shown in Fig. 7a—layers of 10 mil thickness PET provide structural rigidity (avoiding the internal delamination of cardboard under high loading) and a flexural layer of 1 mil thickness PET bonded to 1 mil thickness ripstop nylon provides the advantages of both of these flexure materials. The thin PET layer is flexible enough to allow for free motion of the flexure while stiffening it in shear and compressive loading directions. The thin ripstop nylon fabric layer provides resistance to tearing under high impact forces.

In addition, LoadRoACH has a custom transmission pictured in Fig. 7b that can easily be swapped out and maintained. The dual output crank design is similar to that of X2-VelociRoACH [21], and provides a more robust mechanical transmission of motor torques to leg forces than the planarizing four bar linkage of VelociRoACH. The transmission has two independently actuated outputs that drive left and right leg sets, with encoder feedback on output crank angle. With improved mechanical robustness, the 55 g LoadRoACH robot is able to dynamically run while carrying a tail and shell payload of 27 g.

A picture of the tail module on the robot is shown in Fig. 8a and a solid model representation is shown in Fig. 8b. The thin carbon fiber tail is driven by a 30:1 reduction brushed metal gearmotor (*Pololu*). The magnetic encoder on the back shaft of the motor measures rotation of the motor shaft, and the Hall switch on the front of the motor mount is used to set the tail position relative to the body-fixed vertical.

B. Straight running performance

To benchmark the running performance of LoadRoACH with a tail and shell payload, the robot was run in a motion capture environment (*OptiTrack*). The robot was commanded to follow an alternating tripod gait with stride frequencies ranging from 1 Hz to 10 Hz on carpet, tarp, and loose gravel (with centimeter-scale rocks) surfaces. The average forward velocity of the robot over 5 trials for each experiment condition are shown in Fig. 9. At the fastest trackable stride frequency of 10 Hz, the robot has the highest forward velocity of 72 cm/s on carpet (with a measured leg-ground C.o.F. of 1.25). The robot also runs well on tarp (with a measured leg-ground C.o.F. of 0.65), because its cast polyurethane C-legs have a soft overmolded tread. Straight running velocity significantly decreases to 44 cm/s on gravel, because the robot has to overcome ineffective leg pushes against gravel and body-terrain interaction forces. Compared to the 30 g VelociRoACH running at 10 Hz without an aerodynamic stabilizer [20], LoadRoACH on average runs only 3 cm/s slower on carpet.

V. Tail Contact Turning Experiments

A. Open-loop turning performance

Experimental open-loop turning performance results for differential drive, tail drag, and tail impact turning methods are shown in Fig. 10. The video attachment shows the robot turning with each strategy on carpet. In each of these plots, the horizontal axis is the control parameter modulating the effect of the turning strategy. For differential drive, either the right or left leg side runs at a stride frequency of 10 Hz while the other leg side is decreased to $(8, 5, 2, 0)$ Hz. For tail drag,

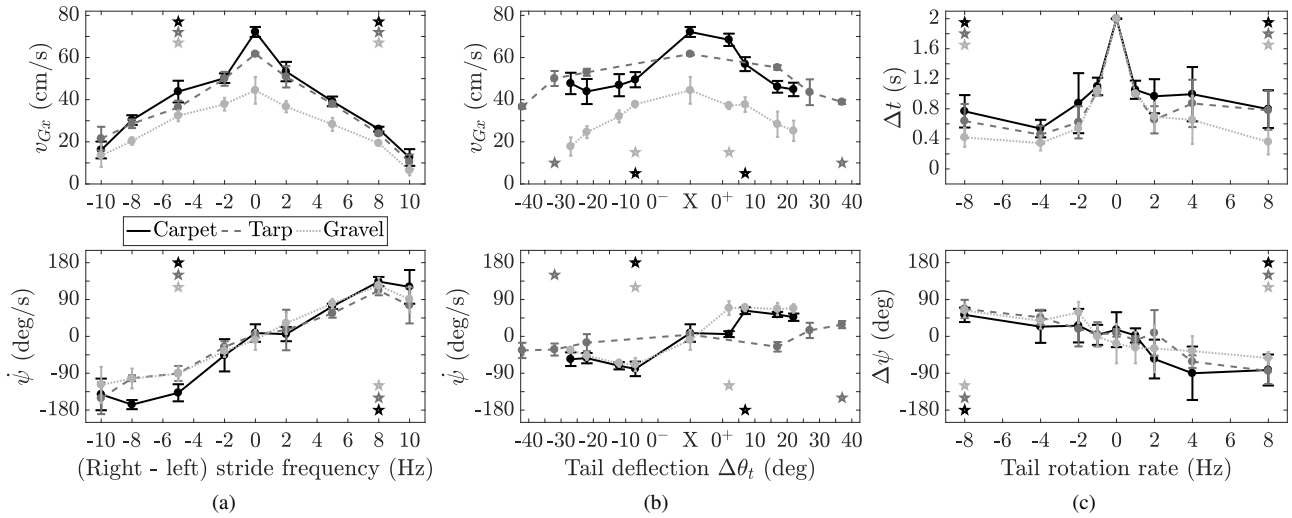

Fig. 10. Forward speed v_{Gx} (measured from motion tracking) and angular rate $\dot{\psi}$ (measured from the robot's gyroscope) of the robot turning with sustained control effort through (a) differential drive and (b) tail drag turning methods. (c) Turn time Δt and turn angle $\Delta\psi$ over a single impact of the tail against the ground with varying tail rotation rate. Each data point gives the experimental mean over at least 4 trials with error bars showing the sample standard deviation. Results are shown for carpet, tarp, and gravel surfaces. The stars mark the highest performance turn with regard to average maneuverability $v_{Gx}\dot{\psi}$ for differential drive and tail drag turning, and average angular velocity over the turn event $\Delta\psi/\Delta t$ for tail impact turning.

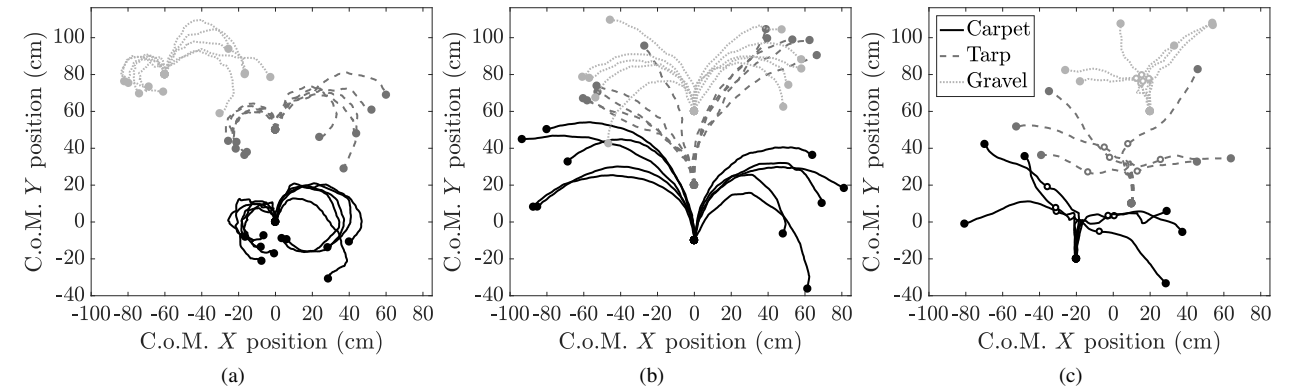

Fig. 11. Experimental center of mass trajectories (measured from motion tracking) for turns with the highest performance metrics. Individual trials on different surfaces are shown for (a) differential drive, (b) tail drag, and (c) tail impact turning methods.

the robot runs using an alternating tripod gait with a stride frequency of 10 Hz and controls the position of its tail to apply up to a $40°$ tail deflection, where a negative value of $\Delta\theta_t$ indicates that the tail touches down clockwise on the ground (opposite to Fig. 2). For tail impact, the robot runs using a 10 Hz alternating tripod gait and then impacts its tail against the ground once, with a controlled tail rotation rate varying from 1 Hz to 8 Hz (positive is counterclockwise).

The differential drive (Fig. 10a) and tail drag (Fig. 10b) turning strategies produce sustained turns. As expected, a positive stride frequency difference and a positive tail deflection produce counterclockwise turns (positive $\dot{\psi}$), and the direction of the turn can be changed by switching the sign of the control action. In comparison to the analysis, the fastest experimental tail drag turn condition ($\Delta\theta_t = -7°$ on carpet) had an average forward velocity of 49 cm/s (84% of the analytical value) and an average angular velocity of -79 deg/s, which corresponds to the analytical projection scaled by an aerial duty factor of $D_{aerial} = 0.44$. Increasing tail deflection causes the forward and angular velocity to decrease, but turning for $\Delta\theta_t$ past $\pm 25°$ is not accurately modeled.

TABLE I

MAXIMUM SUSTAINED TURNING MANEUVERABILITY

Γ (deg m/s^2)	Carpet	Tarp	Gravel
Differential drive	$(-60, 35)$	$(-33, 27)$	$(-29, 24)$
Tail drag	$(-39, 36)$	$(-13, 11)$	$(-26, 26)$

A relevant turning performance metric is maneuverability $\Gamma = v_{Gx}\dot{\psi}$. Turns with higher Γ allow the robot to redirect its heading quickly while maintaining a high forward speed. The starred test conditions in Fig. 10 produced the highest maneuverability turns, and the resulting turn trajectories are shown in Fig. 11. Table I shows the maximum sustained turning maneuverability for clockwise and counterclockwise turns (negative indicates clockwise, positive indicates counterclockwise). For the carpet and gravel surfaces, tail drag and differential drive turns have similar maneuverability, with the exception of clockwise differential drive producing turns

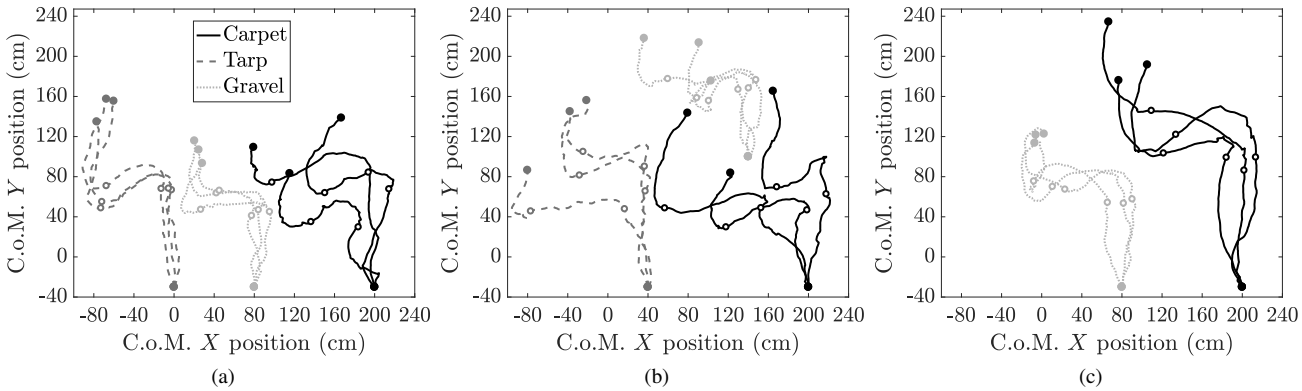

Fig. 12. Closed-loop corner turn steering trajectories using gyroscope feedback. The reference yaw trajectory is 0 degrees from the start, then 90 degrees counterclockwise, then 0 degrees until the end. The white circles indicate a step change in reference heading. (a) Differential drive, (b) differential drive with tail impact switching, and (c) tail drag with tail impact switching steering methods.

with almost 50% higher maneuverability than clockwise tail drag. This asymmetric turning behavior can be explained by construction differences in the left and right sides of the robot's legs and transmission. Tail drag turning on tarp produces far less maneuverable turns than differential drive, which is due to the tail's limited friction (measured C.o.F. of 0.35 compared to the value of 0.7 on carpet) producing smaller yaw moments.

While the differential drive and tail drag turns have a similar value of Γ on carpet, they produce significantly different turns, as illustrated in the trajectories in Fig. 11a and Fig. 11b. Differential drive produces tighter turns with lower forward velocity, and tail drag produces lower curvature turns with higher forward velocity. These two different types of turning could be combined to enable the robot to select a strategy for different types of trajectory following tasks.

The tail impact turning performance (Fig. 10c) is determined by the net yaw heading change $\Delta\psi$ that the turn produces and the elapsed time Δt for the robot to reach its nominal average forward running velocity (from Fig. 9) after the start of the tail impact. Overall, faster tail rotation rates produce faster changes in heading $\Delta\psi/\Delta t$. Counterclockwise tail impacts produce clockwise turns and vice versa, which is consistent with the time series data in Fig. 6. Fig. 11c shows a selection of the fastest clockwise and counterclockwise tail impact turns (the filled white circles indicate the robot's C.o.M. position at which it reached its nominal average forward velocity after the tail impact). Note that some trajectories were omitted in this plot (but not from the net statistics in Fig. 10c) because the robot did not turn in the intended direction. The achievable reorientation angles are similar across carpet, tarp, and gravel surfaces, and the robot takes a shorter average time to reorient on gravel, in which the robot is traveling at lower forward velocities. There is large variability in $\Delta\psi$ and Δt, because the magnitude of the rotation effect of the tail impact and the interaction of the legs with the ground depends heavily on the state of the robot at the instant of tail impact. Tail impact turning provides a rapid yaw reorientation capability with a smaller turn radius than differential drive or tail drag turning, but the consistency of the strategy needs to be improved.

B. Closed-loop steering

The three turning methods characterized in the previous subsection were implemented in an aggressive closed-loop steering maneuver with feedback on the robot's gyroscope state giving yaw heading. Representative clips of each maneuver are included in the video attachment. Fig. 12 compares three steering strategies—differential drive, differential drive with tail impact past an angular error threshold, and tail drag turning with tail impact. Note that the robot is not using information from the motion tracking system to follow absolute position trajectories. Differential drive was continuously modulated using a PID controller on heading with one side running at a 10 Hz stride frequency and the other side decreasing down to 2 Hz. Tail drag was continuously modulated using a PID controller on heading by varying the duty cycle of tail contact on the ground with the most effective turning deflections selected from Fig. 10b. Tail impact occurred by switching the tail control to track a rotation rate of ± 4 Hz whenever the yaw error exceeded a threshold of $\mp 70^\circ$. For the tail steering strategies, the robot ran at maximum speed with a 10 Hz alternating tripod gait.

The steering performance during the aggressive corner turn maneuver for each closed-loop strategy is shown in Fig. 13. The two performance metrics are the root mean square yaw error in tracking the trajectory and the average velocity of the robot along the desired direction over the course of steering. All test conditions produced large RMS yaw errors ranging from 30° to 45°. The one noticeable improvement in steering is that the tail drag with tail impact control strategy implemented on carpet produces a 30% higher speed towards goal (40 cm/s) compared to differential drive (30 cm/s). As shown in Fig. 12, differential drive produces large oversteering swings on carpet, which can be explained by the continuously varying phasing of the legs as the robot changes leg velocity. In contrast, tail drag turning produces more gradual heading adjustments during straight segments, while tail impacts rapidly change heading during corner transitions.

VI. Conclusions

LoadRoACH, a palm-sized legged robot with increased payload capacity was developed to test novel turning strate-

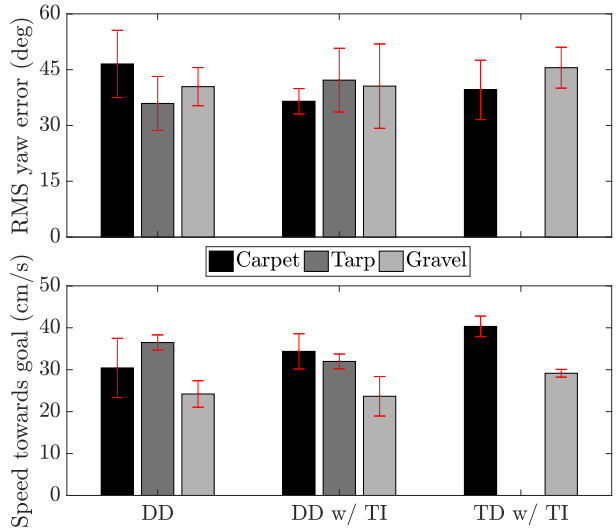

Fig. 13. Closed-loop steering performance for an aggressive corner turn maneuver. The mean and standard deviation of 3 trials are shown for differential drive (DD), differential drive with tail impact (DD w/ TI), and tail drag with tail impact (TD w/ TI) control strategies.

gies leveraging contact with an active tail. In an analysis of the steady-state turns that can be sustained by a dragging tail, a bound on the forward and angular velocity of tail drag turning on carpet was determined and experimentally validated. In open-loop turning experiments, the tail drag method exhibited comparable turning maneuverability relative to the baseline of differential drive on carpet and gravel surfaces, and was not able to produce significant turns on a tarp surface with low friction. In addition, the tail impact turning strategy produced rapid heading changes on carpet, tarp, and gravel, albeit with significant variability in the turn angle and the time to recover forward velocity after tail impact. In a closed-loop steering test of the robot tracking an aggressive corner turn, tail contact turning demonstrated an improvement in steering performance on carpet compared to differential drive. By combining tail drag modulated steering with transient tail impacts to correct large heading errors, the robot was able to complete the corner turn maneuver while progressing faster towards the instantaneous goal heading. These closed-loop steering tests featured LoadRoACH operating at the upper limits of its forward and turning velocity. Better and more consistent steering performance could be achieved in trajectory tracking tasks with lower forward speeds and more gradual heading changes.

In future work, a scaling relation for the maximum achievable stride frequency and forward velocity for legged robots running with payload will be derived based on the power requirements, friction limitations, and dynamics of legged running. The tail drag equilibrium analysis will be applied in a sensitivity study to determine the space of possible turns with different tail geometries, robot drive capabilities, and environment friction conditions. In addition, tail impact control strategies other than following a fixed velocity trajectory will be explored. More consistent tail impact turning effects could be achieved by modulating the tail effort according to feedback controllers that consider the estimated torque exerted by the tail and the measured state information from the robot's IMU and leg encoders. Finally, the closed-loop steering capabilities of tail contact turning combined with various legged gaits will be further characterized in gradual to aggressive turning trajectories.

Acknowledgments

Thanks to Scout Heid for initial transmission design work.

References

[1] U. Saranli, M. Buehler, and D. E. Koditschek, "RHex: A simple and highly mobile hexapod robot," *Int. J. Robot. Res.*, vol. 20, no. 7, pp. 616–631, 2001.

[2] M. Raibert, K. Blankespoor, G. Nelson, and R. Playter, "BigDog, the rough-terrain quadruped robot," *IFAC Proceedings Volumes*, vol. 41, no. 2, pp. 10 822–10 825, 2008.

[3] H.-W. Park, P. M. Wensing, and S. Kim, "High-speed bounding with the MIT Cheetah 2: Control design and experiments," *Int. J. Robot. Res.*, vol. 36, no. 2, pp. 167–192, 2017.

[4] C. S. Casarez and R. S. Fearing, "Dynamic terrestrial self-righting with a minimal tail," in *IEEE/RSJ IROS*, 2017, pp. 314–321.

[5] A. T. Baisch, O. Ozcan, B. Goldberg, D. Ithier, and R. J. Wood, "High speed locomotion for a quadrupedal microrobot," *Int. J. Robot. Res.*, vol. 33, no. 8, pp. 1063–1082, 2014.

[6] S. Kim, J. E. Clark, and M. R. Cutkosky, "iSprawl: Design and tuning for high-speed autonomous open-loop running," *Int. J. Robot. Res.*, vol. 25, no. 9, pp. 903–912, 2006.

[7] A. O. Pullin, N. J. Kohut, D. Zarrouk, and R. S. Fearing, "Dynamic turning of 13 cm robot comparing tail and differential drive," in *IEEE ICRA*, 2012, pp. 5086–5093.

[8] A. M. Hoover, S. Burden, X.-Y. Fu, S. S. Sastry, and R. S. Fearing, "Bio-inspired design and dynamic maneuverability of a minimally actuated six-legged robot," in *IEEE/RAS-EMBS Int. Conf. Biomed. Robot. Biomechatronics*, 2010, pp. 869–876.

[9] D. W. Haldane and R. S. Fearing, "Roll oscillation modulated turning in dynamic millirobots," in *IEEE ICRA*, 2014, pp. 4569–4575.

[10] D. Zarrouk and R. S. Fearing, "Controlled in-plane locomotion of a hexapod using a single actuator," *IEEE Trans. Robot.*, vol. 31, no. 1, pp. 157–167, 2015.

[11] N. J. Kohut, A. O. Pullin, D. W. Haldane, D. Zarrouk, and R. S. Fearing, "Precise dynamic turning of a 10 cm legged robot on a low friction surface using a tail," in *IEEE ICRA*, 2013, pp. 3299–3306.

[12] A. Patel and M. Braae, "Rapid turning at high-speed: Inspirations from the cheetah's tail," in *IEEE/RSJ IROS*, 2013, pp. 5506–5511.

[13] N. J. Kohut, D. Zarrouk, K. C. Peterson, and R. S. Fearing, "Aerodynamic steering of a 10 cm high-speed running robot," in *IEEE/RSJ IROS*, 2013, pp. 5593–5599.

[14] T. Libby, A. M. Johnson, E. Chang-Siu, R. J. Full, and D. E. Koditschek, "Comparative design, scaling, and control of appendages for inertial reorientation," *IEEE Trans. Robot.*, vol. 32, no. 6, pp. 1380–1398, 2016.

[15] D. W. Haldane, M. M. Plecnik, J. K. Yim, and R. S. Fearing, "Robotic vertical jumping agility via series-elastic power modulation," *Science Robotics*, vol. 1, no. 1, 2016.

[16] C. C. Kessens, C. T. Lennon, and J. Collins, "A metric for self-rightability and understanding its relationship to simple morphologies," in *IEEE/RSJ IROS*, 2014, pp. 3699–3704.

[17] C. Li, C. C. Kessens, R. S. Fearing, and R. J. Full, "Mechanical principles of dynamic terrestrial self-righting using wings," *Advanced Robotics*, vol. 31, no. 17, pp. 881–900, 2017.

[18] A. L. Brill, A. De, A. M. Johnson, and D. E. Koditschek, "Tail-assisted rigid and compliant legged leaping," in *IEEE/RSJ IROS*, 2015, pp. 6304–6311.

[19] P. Birkmeyer, K. Peterson, and R. S. Fearing, "DASH: A dynamic 16g hexapedal robot," in *IEEE/RSJ IROS*, 2009, pp. 2683–2689.

[20] D. W. Haldane, K. C. Peterson, F. L. Garcia Bermudez, and R. S. Fearing, "Animal-inspired design and aerodynamic stabilization of a hexapedal millirobot," in *IEEE ICRA*, 2013, pp. 3279–3286.

[21] D. W. Haldane and R. S. Fearing, "Running beyond the bio-inspired regime," in *IEEE ICRA*, 2015, pp. 4539–4546.